THE CLOSEST POINT METHOD AND MULTIGRID SOLVERS FOR ELLIPTIC EQUATIONS ON SURFACES

YUJIA CHEN   AND   COLIN B. MACDONALD*

Abstract. Elliptic partial differential equations are important both from application and analysis points of views. In this paper we apply the Closest Point Method to solve elliptic equations on general curved surfaces. Based on the closest point representation of the underlying surface, we formulate an embedding equation for the surface elliptic problem, then discretize it using standard finite differences and interpolation schemes on banded, but uniform Cartesian grids. We prove the convergence of the difference scheme for the Poisson's equation on a smooth closed curve. In order to solve the resulting large sparse linear systems, we propose a specific geometric multigrid method in the setting of the Closest Point Method. Convergence studies both in the accuracy of the difference scheme and the speed of the multigrid algorithm show that our approaches are effective.

Key words. Surface elliptic problem, Surface Poisson problem, Laplace–Beltrami operator, Closest Point Method, Geometric multigrid method.

AMS subject classifications. 58J05, 65N06, 65N55

1. Introduction. Partial differential equations (PDEs) on surfaces are important for many applications in engineering [25], material science [26], biology [22], and image processing [28]. In all these applications, numerical algorithms are essential for solving PDEs. There are a variety of techniques for solving surface PDEs numerically, typically depending on the geometrical representation of the underlying surface:

- One can find a parametrization of the surface [11], formulate and solve the PDE in the parameter space.
- One can also find a triangulation or a polygonal approximation of the surface, and solve the PDE on the approximated surface by finite differences [29] or finite elements [7, 8].
- Based on a level set representation of the surface, one can formulate an embedding PDE corresponding to the surface PDE, then use either finite differences [2, 13] or finite elements [5, 9, 6] to numerically solve the PDE in the embedding space. This level set approach is desirable for PDEs on moving surfaces [32, 10].
- Based on a closest point representation of the surface, one can also formulate an embedding equation (in a different way from the level set approach), then solve the embedding equation in a banded, uniform Cartesian grid with finite differences [24, 19, 20]. This approach is called the Closest Point Method.
- Starting from a point cloud (supposed to be sampled from the surface), one can reconstruct the surface by radial basis functions, and solve the PDE on the reconstructed surface via the radial basis function finite difference method [23, 12]. There are also other approaches to compute on point clouds with no reconstruction procedure [18] or with only local reconstruction [16].

In this paper we will adopt the Closest Point Method, and focus on solving elliptic PDEs on surfaces. Similarly to the level set approach, the Closest Point Method extends the surface PDE to the embedding space of the surface in such a way that the embedding equation agrees with the original PDE on the surface. However, the

Closest Point Method extends the solution via the *closest point extension* so that the extended solution is constant along the normals to the surface, and thus the Cartesian differential operators agree with the surface intrinsic differential operators on the surface. One does not need to modify the Cartesian differential operators as in the case of the level set approach.

The Closest Point Method has been successfully applied to solving a wide variety of time-dependent PDEs [24, 19, 20] and eigenvalue problems for the Laplace–Beltrami operator [17] on surfaces, but less attention has been paid to solving elliptic problems. Motivated by constructing implicit schemes for the in-surface heat equation, Macdonald and Ruuth [20] propose a way to discretize the embedding operator corresponding to the Laplace–Beltrami operator; this idea is also successfully applied to solving eigenvalue problems for the Laplace–Beltrami operator on surfaces [17]. One can apply the approach in [20, 17] to deal with the elliptic operators, but this requires a properly extended right-hand side function from the surface to the embedding space. A simple closest point extension of the right-hand side seems to work in practice but the resulting schemes are hard to analyze because the solutions are *not* constant in the direction of the normal of the surface. We discuss this further in Section 2.3.

To overcome this issue, we formulate an embedding equation for the surface elliptic problem using a different approach from [20, 17]. The new embedding equation agrees with the original PDE on the surface and has a solution which is constant along the normals to the surface. Similar ideas have been investigated for method-of-lines approaches to solve time-dependent problems involving more general surface differential operators [31], but here we focus on elliptic problems. We then construct a finite difference scheme which is consistent with the embedding equation. Furthermore, for the shifted Poisson's equation on a smooth closed curve embedded in $\mathbb{R}^2$, we prove that the difference scheme is second-order convergent in the ∞-norm under some smoothness assumptions.

The difference scheme yields a sparse linear system. If $\mathcal{S}$ is a curve in $\mathbb{R}^2$, the resulting linear system can be easily solved by sparse direct solvers such as Matlab's backslash; but if $\mathcal{S}$ is a surface in $\mathbb{R}^3$ or higher-dimensional spaces, efficient iterative solvers are needed. We propose a specific geometric multigrid algorithm in the setting of the Closest Point Method, making full use of the closest point representation of the surface and uniform Cartesian grids surrounding the surface.

The rest of the paper is organized as follows. In Section 2 we formulate the embedding equation for the surface elliptic problem. In Section 3 we discretize the embedding equation for the surface Poisson problem, and analyze the difference scheme; we also provide some numerical examples for Poisson equations on closed curves in $\mathbb{R}^2$ to validate our analysis. In Section 4, motivated by solving the large sparse linear systems arising from problems where the embedding space is $\mathbb{R}^3$ or higher, we propose a V-Cycle Multigrid algorithm based on the closest point representation of the surface. We then present examples on various surfaces and with variable diffusion coefficients to show the efficiency of our specific V-Cycle Multigrid algorithm. In Section 5 we draw several conclusions and discuss some future work.

2. Continuous embedding equation.

2.1. Embedding equation for surface Poisson problem. For ease of derivation, we first focus on the shifted Poisson's equation on a smooth closed surface $\mathcal{S}$:

$$-\Delta_{\mathcal{S}} u(\boldsymbol{y}) + c u(\boldsymbol{y}) = f(\boldsymbol{y}), \qquad \boldsymbol{y} \in \mathcal{S}, \tag{2.1}$$

where $f(\boldsymbol{y})$ is a continuous function defined on the surface $\mathcal{S}$, and we assume c to be a positive constant for simplicity.[1] Since $c > 0$, (2.1) has a unique solution.

Because $\mathcal{S}$ is smooth, there is a tubular neighborhood $B(\mathcal{S})$ surrounding $\mathcal{S}$ [15, 21] such that the following function is well defined in $B(\mathcal{S})$. We define the (Euclidean) closest point function cp : $B(\mathcal{S}) \to \mathcal{S}$ such that for each point $\boldsymbol{x} \in B(\mathcal{S})$, cp($\boldsymbol{x}$) is a surface point which is closest to $\boldsymbol{x}$ in Euclidean distance [24]. We want to define an embedding equation in $B(\mathcal{S})$, whose solution agrees with the solution of the surface PDE (2.1) on $\mathcal{S}$.

We construct the right-hand side function $\tilde{f}$ in $B(\mathcal{S})$ via the closest point extension,

$$\tilde{f}(\boldsymbol{x}) = f(\mathrm{cp}(\boldsymbol{x})), \qquad \boldsymbol{x} \in B(\mathcal{S}).$$

From this construction of $\tilde{f}$ and the idempotence of the closest point extension, we have that

$$\tilde{f}(\boldsymbol{x}) = \tilde{f}(\mathrm{cp}(\boldsymbol{x})), \qquad \boldsymbol{x} \in B(\mathcal{S}). \tag{2.2}$$

We also want to find a solution $\tilde{u}$ in the band $B(\mathcal{S})$ which is constant along the normal direction to the surface, i.e., we will need to impose this condition on $\tilde{u}$,

$$\tilde{u}(\boldsymbol{x}) = \tilde{u}(\mathrm{cp}(\boldsymbol{x})), \qquad \boldsymbol{x} \in B(\mathcal{S}). \tag{2.3}$$

Since $\tilde{u}$ is constant along the normal direction to the surface, the Cartesian Laplacian of $\tilde{u}$ equals the Laplace–Beltrami function of $\tilde{u}$ on the surface [24], and thus

$$-\Delta \tilde{u}(\boldsymbol{y}) + c\tilde{u}(\boldsymbol{y}) = \tilde{f}(\boldsymbol{y}), \qquad \boldsymbol{y} \in \mathcal{S}.$$

Replacing $\boldsymbol{y}$ with cp($\boldsymbol{x}$), we have

$$-[\Delta \tilde{u}](\mathrm{cp}(\boldsymbol{x})) + c\tilde{u}(\mathrm{cp}(\boldsymbol{x})) = \tilde{f}(\mathrm{cp}(\boldsymbol{x})), \qquad \boldsymbol{x} \in \mathrm{B}(\mathcal{S}).$$

Here the square bracket $[\cdot]$ surrounding $\Delta\tilde{u}$ means that we first calculate the Cartesian Laplacian of $\tilde{u}(\boldsymbol{x})$, and then evaluate at the closest point of $\boldsymbol{x}$ on the surface. By assumption, both $\tilde{f}$ and $\tilde{u}$ are closest point extensions ((2.2) and (2.3)), so we have

$$-[\Delta \tilde{u}](\mathrm{cp}(\boldsymbol{x})) + c\tilde{u}(\boldsymbol{x}) = \tilde{f}(\boldsymbol{x}), \tag{2.4a}$$
$$\text{subject to} \quad \tilde{u}(\boldsymbol{x}) = \tilde{u}(\mathrm{cp}(\boldsymbol{x})), \quad \boldsymbol{x} \in B(\mathcal{S}). \tag{2.4b}$$

Equation (2.4a) ensures that the embedding equation agrees with the original surface PDE on the surface, and we will call it the *consistency condition*. Equation (2.4b) forces $\tilde{u}$ to be constant along the normal direction to the surface (so that we can replace the surface Laplacian with the Cartesian Laplacian), and we will call it the *side condition*. Combining the two equations (2.4a) and (2.4b), we get the embedding equation,

$$-[\Delta \tilde{u}](\mathrm{cp}(\boldsymbol{x})) + c\tilde{u}(\boldsymbol{x}) + \gamma(\tilde{u}(\boldsymbol{x}) - \tilde{u}(\mathrm{cp}(\boldsymbol{x}))) = \tilde{f}(\boldsymbol{x}), \quad \boldsymbol{x} \in B(\mathcal{S}), \tag{2.5}$$

where γ is a parameter. As we shall show next, the choice of γ does not have much impact on the continuous equation (2.5); but later in our numerical scheme, γ plays a role in balancing the side and consistency conditions.

---

[1] Our derivations and proofs also work for the case where $c(\boldsymbol{y})$ is a surface function satisfying $c(\boldsymbol{y}) \geq C > 0$, where C is a positive constant.

So far we have shown that the system (2.4) leads to equation (2.5). Following the ideas of [31], we are going to show that in the continuous setting and if $\gamma \neq -c$, equation (2.5) implies *both* equations (2.4a) and (2.4b). We rearrange equation (2.5) as

$$- [\Delta \tilde{u} + \gamma \tilde{u}](\mathrm{cp}(\boldsymbol{x})) = \tilde{f}(\boldsymbol{x}) - (\gamma + c)\tilde{u}(\boldsymbol{x}), \quad \boldsymbol{x} \in B(\mathcal{S}). \tag{2.6}$$

Here the square bracket $[\cdot]$ surrounding $\Delta \tilde{u} + \gamma \tilde{u}$ means that we first calculate the Cartesian Laplacian of $\tilde{u}(\boldsymbol{x})$ and add the result with $\gamma \tilde{u}(\boldsymbol{x})$, then evaluate the function $\Delta \tilde{u} + \gamma \tilde{u}$ at the closest point of $\boldsymbol{x}$ on the surface. The left-hand side of equation (2.6) is constant along the direction normal to $\mathcal{S}$, so the right-hand side $\tilde{f}(\boldsymbol{x}) - (\gamma + c)\tilde{u}(\boldsymbol{x})$ also has to be constant along the normal direction to $\mathcal{S}$, i.e.,

$$\tilde{f}(\boldsymbol{x}) - (\gamma + c)\tilde{u}(\boldsymbol{x}) = \tilde{f}(\mathrm{cp}(\boldsymbol{x})) - (\gamma + c)\tilde{u}(\mathrm{cp}(\boldsymbol{x})).$$

Since $\tilde{f}(\boldsymbol{x}) = \tilde{f}(\mathrm{cp}(\boldsymbol{x}))$, if $\gamma \neq -c$, we have that $\tilde{u}(\boldsymbol{x}) = \tilde{u}(\mathrm{cp}(\boldsymbol{x}))$, i.e., equation (2.4b) holds. Substituting (2.4b) back into equation (2.5), we have that equation (2.4a) holds. In other words, from equation (2.5) with $\gamma \neq -c$, we derive that both equations (2.4a) and (2.4b) hold.

In summary, our logic is as follows: in order to solve the original surface PDE (2.1), we seek $\tilde{u}(\boldsymbol{x})$ in $B(\mathcal{S})$ satisfying both the consistency condition (2.4a) and the side condition (2.4b), which is in turn equivalent to equation (2.5) (provided $\gamma \neq -c$). So from now on we can focus on equation (2.5).

2.2. More general elliptic operators. The above ideas extend naturally to more general linear surface elliptic PDEs,

$$- \nabla_{\mathcal{S}} \cdot (\boldsymbol{A}(\boldsymbol{y}) \nabla_{\mathcal{S}} u(\boldsymbol{y})) + c(\boldsymbol{y}) u(\boldsymbol{y}) = f(\boldsymbol{y}), \quad \boldsymbol{y} \in \mathcal{S}, \tag{2.7}$$

where $\boldsymbol{A}(\boldsymbol{y})$ is a symmetric and semi-positive definite matrix.

Again we construct $\tilde{f}(\boldsymbol{x}) = f(\mathrm{cp}(\boldsymbol{x}))$, $\boldsymbol{x} \in B(\mathcal{S})$, and would like to enforce the side condition $\tilde{u}(\boldsymbol{x}) = \tilde{u}(\mathrm{cp}(\boldsymbol{x}))$ for the solution $\tilde{u}$ defined in $B(\mathcal{S})$. Using the generalized closest point principle ([21, Theorem 4.3]), the following equations agree with surface PDE (2.7) on the surface,

$$-[\nabla \cdot (\boldsymbol{A}(\mathrm{cp}(\boldsymbol{x})) \nabla \tilde{u})](\mathrm{cp}(\boldsymbol{x})) + c\tilde{u}(\boldsymbol{x}) = \tilde{f}(\boldsymbol{x}), \tag{2.8a}$$

$$\text{subject to} \quad \tilde{u}(\boldsymbol{x}) = \tilde{u}(\mathrm{cp}(\boldsymbol{x})), \quad \boldsymbol{x} \in B(\mathcal{S}). \tag{2.8b}$$

Here the square bracket $[\cdot]$ surrounding $\nabla \cdot (\boldsymbol{A}(\mathrm{cp}(\boldsymbol{x})) \nabla \tilde{u})$ means that we first perform the gradient on $\tilde{u}$, multiply it by $\boldsymbol{A}(\mathrm{cp}(\boldsymbol{x}))$, then take the divergence, and finally evaluate the results at $\mathrm{cp}(\boldsymbol{x})$. Adding (2.8a) and (2.8b) together, we have

$$-[\nabla \cdot (\boldsymbol{A}(\mathrm{cp}(\boldsymbol{x})) \nabla \tilde{u})](\mathrm{cp}(\boldsymbol{x})) + c\tilde{u}(\boldsymbol{x}) + \gamma(\tilde{u}(\boldsymbol{x}) - \tilde{u}(\mathrm{cp}(\boldsymbol{x}))) = \tilde{f}(\boldsymbol{x}), \quad \boldsymbol{x} \in B(\mathcal{S}), \tag{2.9}$$

Similarly to the Poisson case in Section 2.1, we have the following equivalence relationship.

THEOREM 2.1.
   1. If $\tilde{u} \in B(\mathcal{S})$ is a solution of (2.8), then $\tilde{u}$ is a solution of (2.9).
   2. If $\tilde{u} \in B(\mathcal{S})$ is a solution of (2.9), and $\gamma \neq -c$, then $\tilde{u}$ is a solution of (2.8).
   Proof. The ideas are similar to the Poisson case in Section 2.1, the only difference is that we replace $\Delta \tilde{u}$ with $\nabla \cdot (\boldsymbol{A}(\mathrm{cp}(\boldsymbol{x})) \nabla \tilde{u})$.

We focus our derivation and analysis on the surface Poisson problem via the embedding equation (2.5). In most cases it is straightforward to extend our approach to more general elliptic operators (e.g., we look at variable diffusion coefficients in Section 4.6.6).

As we shall see later in our numerical discretization, by choosing suitable γ in (2.5) we can get a consistent and stable numerical scheme. From (2.5), no boundary conditions for the Laplacian operator are needed at the boundary of the band $B(\mathcal{S})$, since we only need to evaluate $\Delta \tilde{u}$ at the closest points on the surface. We simply need a band large enough to enable this evaluation.

2.3. A comparison with the Macdonald–Brandman–Ruuth approach. If we apply the approach in [20, 17] to the Laplace–Beltrami operator in (2.1), and extend the right hand side via the closest point extension, then we get the following continuous embedding equation,

$$- \Delta(\tilde{u}(\mathrm{cp}(\boldsymbol{x}))) + c\tilde{u}(\boldsymbol{x}) + \gamma(\tilde{u}(\boldsymbol{x}) - \tilde{u}(\mathrm{cp}(\boldsymbol{x}))) = \tilde{f}(\boldsymbol{x}), \quad \boldsymbol{x} \in B(\mathcal{S}). \qquad (2.10)$$

Note that the only difference between (2.5) and (2.10) is that in (2.5) we first perform the Cartesian Laplacian operator on $\tilde{u}$ and then evaluate at $\mathrm{cp}(\boldsymbol{x})$, while in (2.10) we first do the closest point extension of $\tilde{u}$ and then perform the Laplacian. One can show (similarly to [17]), that equation (2.10) agrees with the original surface PDE (2.1) on the surface, and it has a unique solution provided that $\gamma \neq -c$. We can re-arrange (2.10), solving for $\tilde{u}(\boldsymbol{x})$, to obtain

$$\tilde{u}(\boldsymbol{x}) = \frac{1}{c + \gamma} \big(\tilde{f}(\boldsymbol{x}) + \gamma \tilde{u}(\mathrm{cp}(\boldsymbol{x})) + \Delta(\tilde{u}(\mathrm{cp}(\boldsymbol{x}))) \big).$$

From this, $\tilde{u}$ is *not constant along the normals to* $\mathcal{S}$ because $\Delta(\tilde{u}(\mathrm{cp}(\boldsymbol{x})))$ is not constant along the normals. This makes analysis of the method difficult. Furthermore, it would also be difficult to make $\tilde{u}$ constant along the normals to $\mathcal{S}$ by modifying the right-hand side (e.g., via some other method of extension).

In contrast, our new embedding equation (2.5) not only agrees with the original surface PDE (2.1) on the surface, but also has a solution $\tilde{u}$ which is constant in the normal direction to $\mathcal{S}$. The latter property is crucial to the consistency and stability analysis for our numerical discretization in the next section. In addition to these advantages for analysis, (2.5) can lead to a consistent discretization with a sparser coefficient matrix than the one resulting from (2.10); we discuss this further in Remark 3.2. Furthermore, as we shall see in Section 4, the construction of our multigrid solver relies on the property of $\tilde{u}$ being constant along the normal direction to $\mathcal{S}$; it would not be straightforward to design a multigrid solver starting from (2.10) since it gives a solution that is not constant along the normals. Finally, as noted in Section 2.2, our new approach extends naturally to non-constant-coefficient problems.

3. Numerical discretization. Similar to [20], we derive a matrix formulation of a finite difference scheme for the embedding equation (2.5).

3.1. Construction of the difference scheme. Suppose the surface $\mathcal{S}$ is embedded in $\mathbb{R}^d$, and a uniform Cartesian grid is placed in the embedding space. When discretizing $u(\mathrm{cp}(\boldsymbol{x}))$, we need to assign the value at each grid point $\boldsymbol{x}$ to be the value at the corresponding closest point $\mathrm{cp}(\boldsymbol{x})$; since the closest point is generally not a grid point, its value is obtained through interpolation of values at the surrounding grid points. Similarly to [20], we use tensor product Barycentric Lagrange interpolation

Fig. 3.1. *Examples of the lists of grid points B_{interp} (indicated by •) and B_{edge} (indicated by ∘) where the curve $\mathcal{S}$ is a circle. The interpolation stencil is a 4×4 grid (arising, for example, from using degree 3 barycentric Lagrange interpolation) and the shaded regions illustrate the use of this stencil at the three points on the circle indicated by ◇. Five-point difference stencils are shown for two example points in B_{interp}, in one case illustrating the use of points in B_{edge}.*
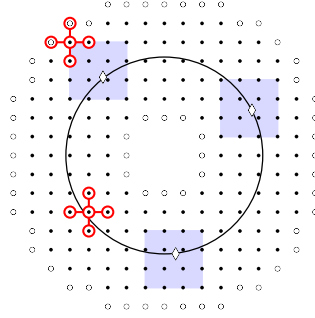
[1], where the interpolated value is a linear combination of the values at neighboring grid points in a hypercube. We call these grid points neighboring the closest point $\text{cp}(\boldsymbol{x})$ the *interpolation stencil* of the scheme.

We also use standard finite difference schemes (e.g., the $\frac{1}{\Delta x^2}\{-4, 1, 1, 1, 1\}$ rule for the Laplacian in 2D), and this requires a *difference stencil* for each grid point.

Let us review the definition of the two lists of discrete points in [20]. The first list $B_{interp} = \{\boldsymbol{x}_1, \boldsymbol{x}_2, ..., \boldsymbol{x}_m\}$ contains every grid point which can appear in the interpolation stencil for some point on the surface $\mathcal{S}$. The second one $B_{edge} = \{\boldsymbol{x}_{m+1}, \boldsymbol{x}_{m+2}, ..., \boldsymbol{x}_{m+m_e}\}$ contains points which are not in B_{interp} but appear in the difference stencil of some point in B_{interp}. Figure 3.1 shows an example of the two lists B_{interp} and B_{edge} where the curve $\mathcal{S}$ is a circle embedded in $\mathbb{R}^2$. Let B be a set of grid points such that $B_{interp} \cup B_{edge} \subseteq B$. Let $n = \|B\|$ be the number of points in B. We introduce the vector $u^h \in \mathbb{R}^n$ with entries $u_i \approx \tilde{u}(\boldsymbol{x}_i)$ for each grid point $\boldsymbol{x}_i \in B$, and similarly, $f^h \in \mathbb{R}^n$ with entries $f_i = \tilde{f}(\boldsymbol{x}_i)$.

There are two closest point extensions in (2.5); we can use different degrees of interpolation for the closest point evaluations of $\Delta\tilde{u}$ and $\tilde{u}$. If we use degree p interpolation for $[\Delta\tilde{u}](\text{cp}(\boldsymbol{x}))$, and degree q interpolation for $\tilde{u}(\text{cp}(\boldsymbol{x}))$, then for each grid point $\boldsymbol{x}_i \in B$, we have the following discretized equation,

$$-\sum_{\boldsymbol{x}_j \in \mathrm{I}_p(\text{cp}(\boldsymbol{x}_i))} \omega_j \left(\sum_{\boldsymbol{x}_k \in \mathrm{Diff}(\boldsymbol{x}_j)} l_k u_k \right) + c u_i + \gamma \left(u_i - \sum_{\boldsymbol{x}_j \in \mathrm{I}_q(\text{cp}(\boldsymbol{x}_i))} \bar{\omega}_j u_j \right) = f_i. \quad (3.1)$$

Here $\mathrm{I}_p(\text{cp}(\boldsymbol{x}_i))$ is the degree p interpolation stencil for point $\text{cp}(\boldsymbol{x}_i)$, $\mathrm{Diff}(\boldsymbol{x}_j)$ is the difference stencil for point x_j, and $\mathrm{I}_q(\text{cp}(\boldsymbol{x}_i))$ is the degree q interpolation stencil for point $\text{cp}(\boldsymbol{x}_i)$; ω_j are the weights of the interpolation scheme for evaluating $[\Delta\tilde{u}](\text{cp}(\boldsymbol{x}))$, $\bar{\omega}_j$ are the weights of the interpolation scheme for evaluating $\tilde{u}(\text{cp}(\boldsymbol{x}))$, and l_k are the weights for the difference scheme approximating the Laplacian operator.

Since the interpolation and difference schemes are linear combinations of the entries of u^h, we can write equation (3.1) in matrix form. Denote the discrete solution by a column vector u^h, the discrete right-hand side function by a vector f^h, the identity matrix by I^h, the closest point interpolation matrices of degree p and q by E_p^h and E_q^h, and the discrete Laplace matrix by L^h. The matrix form of the difference scheme for the embedding equation (2.5) is

$$-E_p^h L^h u^h + c u^h + \gamma (I^h - E_q^h) u^h = f^h. \quad (3.2)$$

We recall that the points in B_{edge} do not belong to any of the interpolation stencils, which means that the columns in E_p^h corresponding to points in B_{edge} are all zero

columns, so the rows in L^h corresponding to points in B_{edge} can vary arbitrarily while $E_p^h L^h$ stays unchanged. Thus we see that no boundary condition for the discrete Laplace matrix is needed, since the discrete Laplacian at any points in B_{edge} does not contribute to the closest point evaluation of $L^h u^h$.

As mentioned before, γ is a parameter balancing the side and consistency conditions. As pointed out in [20], a typical choice of γ is $\frac{2d}{\Delta x^2}$, where d is the dimension of the embedding space and Δx is the grid size. In [20], this choice of γ is motivated by stabilizing the implicit time-stepping scheme for the in-surface heat equation.

The choice of $\gamma = \frac{2d}{\Delta x^2}$ is not obvious simply from (3.2), but it turns out to be a good choice there. In Section 3.3 we show that for the shifted Poisson's equation on a closed curve embedded in $\mathbb{R}^2$, the coefficient matrix corresponding to (3.2) is diagonally dominant by rows when we choose $\gamma = \frac{2d}{\Delta x^2}$, $p = 1$, $q = 3$, and L^h as the Laplacian matrix from the standard centered finite difference scheme.

3.2. Truncation error. In this section, we show that the difference scheme (3.2) is consistent for the embedding equation (2.5) provided that $\tilde{u}$ is sufficiently differentiable.

We denote the restriction operator which evaluates the continuous function at the grid points by R^h, and denote the coefficient matrix in the difference scheme (3.2) by A^h, i.e.,

$$A^h = cI^h - M^h, \quad \text{where} \quad M^h = E_p^h L^h - \gamma(I^h - E_q^h). \tag{3.3}$$

Then we prove a theorem showing the form of the truncation error.

THEOREM 3.1. *Assume that $\tilde{u} \in C^k(\mathbb{R}^d)$ is a solution of (2.5), where d is the dimension of the embedding space and $k \geq \max\{4, p+3, q+1\}$ (p and q are the polynomial interpolation degrees for the discrete closest point extension of $\Delta \tilde{u}$ and $\tilde{u}$ respectively). Let L^h be a second-order (in the ∞-norm) approximation to the Cartesian Laplacian Δ, and $\gamma = O(\frac{1}{\Delta x^2})$. We have the following form of the truncation error,[2]*

$$A^h R^h \tilde{u}(x) - R^h \tilde{f}(x) = O(\Delta x^{p+1}) + O(\Delta x^{q-1}) + O(\Delta x^2), \tag{3.4}$$

where A^h is as given in (3.3), and R^h is the restriction operator mentioned before.

Proof. Let $w(x) = \Delta \tilde{u}(x)$, $x \in B(\mathcal{S})$; then $w(x) \in C^{k-2}(\mathbb{R}^d)$. As mentioned before, since $\tilde{u}$ is constant along directions normal to $\mathcal{S}$, $w(y) = \tilde{f}(y)$ for any $y \in \mathcal{S}$. We evaluate w at the closest points on $\mathcal{S}$ through degree p interpolation, which will introduce an interpolation error. Since $k \geq p+3$, $k-2 \geq p+1$, we have the following standard error estimate for degree p polynomial interpolation,

$$E_p^h R^h w(x) - R^h \tilde{f}(x) = O(\Delta x^{p+1}). \tag{3.5}$$

Furthermore, since $\tilde{u} \in C^k(\mathbb{R}^d)$, $k \geq 4$, the Laplacian matrix L^h is a second-order approximation to Δ, we have that

$$R^h w(x) = L^h R^h \tilde{u}(x) + O(\Delta x^2). \tag{3.6}$$

Plugging (3.6) into (3.5), we get

$$E_p^h(L^h R^h \tilde{u}(x) + O(\Delta x^2)) - R^h \tilde{f}(x) = O(\Delta x^{p+1}),$$

---

[2]If $\boldsymbol{v}$ is a column vector, then by $\boldsymbol{v} = O(\Delta x^k)$ we mean that $\|\boldsymbol{v}\|_\infty \leq C\Delta x^k$, where k and C are positive constants.

Since we are using local polynomial interpolation, $\|E_p^h\|_\infty$ is bounded above by some constant independent of Δx, so $E_p^h O(\Delta x^2) = O(\Delta x^2)$; and thus we get

$$E_p^h L^h R^h \tilde{u}(x) - R^h \tilde{f}(x) = O(\Delta x^{p+1}) + O(\Delta x^2). \tag{3.7}$$

Finally, we estimate the error of evaluating $\tilde{u}(\mathrm{cp}(x))$ by degree q interpolation. Because $\tilde{u} \in C^k(\mathbb{R}^d)$ and $k \geq q+1$, once again we have the standard interpolation error estimation,

$$(I^h - E_q^h)R^h \tilde{u}(x) = O(\Delta x^{q+1}). \tag{3.8}$$

Multiplying equation (3.8) by $\gamma = O(\frac{1}{\Delta x^2})$ and adding the results with equation (3.7), we have that equation (3.4) holds. ∎

REMARK 3.2. *According to (3.4), if we pick $p = 1$, $q = 3$, we will get a difference scheme for the embedding equation (2.5) with second-order truncation error in the ∞-norm. Contrasting this discretization with the method of Macdonald–Brandman– Ruuth [17, 20], we note that discretizing (2.10) to second-order consistency requires cubic interpolations in* both *terms. Because lower degree interpolations have smaller stencils, a discretization of (2.5) will yield a coefficient matrix that is sparser than that of (2.10). For example, for a curve in 2D, our new approach is roughly 34% sparser and 50% for a surface in 3D.*

3.3. Convergence for a closed curve in 2-D. In this section, we aim to prove convergence of the difference scheme (3.2) in the restricted case of a closed curve in 2D.

THEOREM 3.3. *Suppose that we wish to solve the embedding equation (2.5) on a smooth closed curve in $\mathbb{R}^2$, and the solution $\tilde{u}$ of the embedding equation satisfies the assumptions in Theorem 3.1. If in (3.2) we choose $\gamma = \frac{4}{\Delta x^2}$, $p = 1$, $q = 3$, and L^h as the Laplacian matrix from the standard $\frac{1}{\Delta x^2}\{-4, 1, 1, 1, 1\}$ finite difference stencil, then the difference scheme (3.2) is second-order convergent in the ∞-norm.*

If the embedding space is $\mathbb{R}^2$, when picking $\gamma = \frac{4}{\Delta x^2}$, and $p = 1$, $q = 3$, the coefficient matrix becomes

$$A^h = cI^h - M^h, \quad \text{where} \quad M^h = E_1^h L^h - \frac{4}{\Delta x^2}(I^h - E_3^h). \tag{3.9}$$

We prove Theorem 3.3 using the following theorem and two propositions.

THEOREM 3.4. *If the embedding space is $\mathbb{R}^2$, then A^h defined by (3.9) (i.e., $\gamma = \frac{4}{\Delta x^2}$, $p = 1$, $q = 3$, and L^h is the Laplacian matrix from the standard $\frac{1}{\Delta x^2}\{-4, 1, 1, 1, 1\}$ finite difference stencil) is an M-Matrix, with positive diagonal entries $a_{kk} > 0$, non- positive off-diagonal entries $a_{kj} \leq 0$, $k \neq j$, and each row sums up to c:*

$$a_{kk} + \sum_{k \neq j} a_{kj} = c. \tag{3.10}$$

PROPOSITION 3.5. *(Varah 1975 [30]) Assume that A is diagonally dominant by rows and set $c = \min_k(|a_{kk}| - \sum_{j \neq k} |a_{kj}|)$. Then $\|A^{-1}\|_\infty \leq 1/c$.*

PROPOSITION 3.6. *If $\|(A^h)^{-1}\|_\infty \leq 1/c$, then the difference scheme (3.2) is second-order convergent in the ∞-norm provided that the scheme has second-order truncation error in the ∞-norm.*

Theorem 3.4 indicates that the coefficient matrix A^h satisfies the assumption of Proposition 3.5, which means that the claim of Proposition 3.5 holds: $\|(A^h)^{-1}\|_\infty \leq 1/c$; and this is in turn the assumption of Proposition 3.6, so the claim of Proposition 3.6 holds. Putting the theorem and propositions together, Theorem 3.3 holds.

Proof of Proposition 3.6. Choosing $p = 1$, $q = 3$, the truncation error estimate (3.4) becomes $A^h R^h \tilde{u}(x) - R^h \tilde{f}(x) = O(\Delta x^2)$. From the discrete linear system (3.2) we have that $A^h u^h - R^h \tilde{f}(x) = 0$. Subtracting these two results gives $A^h(u^h - R^h \tilde{u}(x)) = O(\Delta x^2)$. Because the ∞-norm of $(A^h)^{-1}$ is bounded by a positive constant $1/c$, which is independent of Δx, we get $u^h - R^h \tilde{u}(x) = (A^h)^{-1} O(\Delta x^2) = O(\Delta x^2)$, i.e., the difference scheme (3.2) is second-order convergent in the ∞-norm. ∎

Proof of Theorem 3.4. The proof contains two steps.

Step 1. We first show that *each row of M^h sums up to zero.*

Taking all u_i to be 1 in equation (3.1), the left-hand side minus c becomes

$$- \sum_{x_j \in I_p(\mathrm{cp}(x_i))} \omega_j \left(\sum_{x_k \in \mathrm{Diff}(x_j)} l_k \right) + \gamma \left(1 - \sum_{x_m \in I_q(\mathrm{cp}(x_i))} \bar{\omega}_m \right). \qquad (3.11)$$

Consistency of the finite difference scheme implies that $\sum_{x_k \in \mathrm{Diff}(x_j)} l_k = 0$, for any $x_j \in L$. By the construction of the interpolation weights, $\sum_{x_m \in I_q(\mathrm{cp}(x_i))} \bar{\omega}_m = 1$. So (3.11) equals 0, i.e., each row of M^h sums up to zero.

Step 2. We then prove that *all the off-diagonal entries of M^h are non-negative*, thus all the diagonal entries are non-positive since each row of M^h sums up to zero. For convenience (not necessity) we first rearrange M^h as

$$M^h = E_1^h \left(L^h + \frac{4}{\Delta x^2} I^h \right) + \frac{4}{\Delta x^2} (E_3^h - E_1^h) - \frac{4}{\Delta x^2} I^h.$$

(a) Relative position of the closest point ◇ in the stencil

(b) Local index for points in the stencil

(c) Signs of the weights of bi-cubic interpolation for the closest point ◇
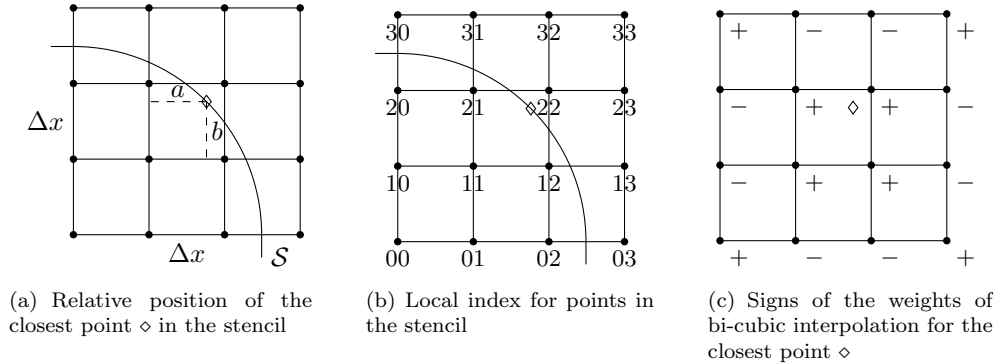
FIG. 3.2. *Information for a 4×4 stencil surrounding the closest point ◇.*

We then investigate the result of multiplying the i-th row of M^h by the column vector u^h. Figure 3.2(a) shows the position of $\mathrm{cp}(\boldsymbol{x}_i)$ (indicated by ◇). $\mathrm{cp}(\boldsymbol{x}_i)$ is in the middle block of the bi-cubic interpolation stencil, and its relative position in the stencil is as shown in Figure 3.2(a). For clarity of notation, we number the points in the bi-cubic interpolation stencil by a local index as shown in Figure 3.2(b). Denote the points in the stencil with respect to the local index by X_{lm} $(0 \le l, m \le 3)$, the corresponding values at these points by U_{lm} $(0 \le l, m \le 3)$, the bi-cubic interpolation weights at points X_{lm} by $\bar{\omega}_{lm}$ $(0 \le l, m \le 3)$, and the bi-linear interpolation weights

at points X_{nk} by ω_{nk} $(0 \le n, k \le 1)$. The i-th entry of $M^h u^h$ becomes

$$\omega_{11}(U_{10} + U_{01} + U_{12} + U_{21})/\Delta x^2$$
$$+\omega_{12}(U_{11} + U_{02} + U_{13} + U_{22})/\Delta x^2$$
$$+\omega_{21}(U_{20} + U_{11} + U_{22} + U_{31})/\Delta x^2$$
$$+\omega_{22}(U_{21} + U_{12} + U_{23} + U_{32})/\Delta x^2$$
$$+4\Big(\sum_{0 \le l,m \le 3} \bar{\omega}_{lm} U_{lm} - \sum_{1 \le l,m \le 2} \omega_{lm} U_{lm} \Big)/\Delta x^2 - 4u_i^h/\Delta x^2. \tag{3.12}$$

By the notation mentioned before, U_{lm} $(0 \le l, m \le 3)$ are just the values of u^h at the points in the bi-cubic interpolation stencil written in the local index. The point $\boldsymbol{x}_i$ might not be contained in the interpolation stencil, so we still write u_i^h in its global index. As l, m go from 1 to 3, X_{lm} might or might not be $\boldsymbol{x}_i$, depending on whether the grid point $\boldsymbol{x}_i$ is in the interpolation stencil of $\mathrm{cp}(\boldsymbol{x}_i)$ or not. In either case the negative coefficient of u_i^h only contributes to the diagonal entry in the corresponding row of the matrix M^h, but the coefficient does not contribute to the off-diagonal entries of M^h. So we only need to show that *all the coefficients of U_{lm}, excluding the potential contribution from the negative coefficient of u_i^h, are non-negative for all* $0 \le l, m \le 3$.

If $\mathrm{cp}(\boldsymbol{x}_i)$ coincides with some grid point $\boldsymbol{x}_j$, then all the interpolation weights vanish except that the weight at $\boldsymbol{x}_j$ is 1, so it is obvious that the above claim is true. Now we only consider cases where $\mathrm{cp}(\boldsymbol{x}_i)$ does not coincide with any grid point, which is the case illustrated in Figure 3.2.

In the rest of the proof, it might be helpful to keep in mind the signs of the bi-cubic interpolation weights $\bar{\omega}_{lm}$ $(0 \le l, m \le 3)$ for $\mathrm{cp}(\boldsymbol{x}_i)$ at each point of the stencil. Figure 3.2(c) shows the signs of the bi-cubic interpolation weights for $\mathrm{cp}(\boldsymbol{x}_i)$ (indicated by $\diamond$) which is in the middle block of the bi-cubic interpolation stencil. These signs can be obtained by straightforward computations, and they do not depend on the precise location of $\mathrm{cp}(\boldsymbol{x}_i)$. Since we interpolate in a dimension-by-dimension fashion, the weights at each of the points are obtained by multiplication of the corresponding weights in the x and y directions. For instance, if we want to compute the bi-cubic interpolation weight at the lower-left corner point $\bar{\omega}_{00}$, we first compute the weight in the x direction, $\bar{\omega}_{00}^x = -\frac{a(\Delta x - a)(2\Delta x - a)}{6\Delta x^3}$, and the weight in the y direction, $\bar{\omega}_{00}^y = -\frac{b(\Delta x - b)(2\Delta x - b)}{6\Delta x^3}$, and then we multiply the weights in the two directions to get $\bar{\omega}_{00} = \bar{\omega}_{00}^x \bar{\omega}_{00}^y$. Here we have used the superscripts x and y in the notations $\bar{\omega}_{00}^x$ and $\bar{\omega}_{00}^y$ to indicate the weights in the x and y directions, respectively. We shall use this notation in the following proof. The bi-cubic weights at other points, and the bilinear weights, can be computed in the same way. Some of their values will be presented in the rest of the proof when necessary.

Now let us finish the proof by calculating the coefficients of U_{lm}. There are three cases for the coefficients of U_{lm} as l, m go from 1 to 3. We only need to verify that for each of the three cases, the coefficients of U_{lm} are positive.

1. Four corner points: $(l, m) = (0, 0), (0, 3), (3, 0), (3, 3)$.
   The only contribution for the row entries corresponding to these four points are the bi-cubic interpolation weights $\bar{\omega}_{00}, \bar{\omega}_{03}, \bar{\omega}_{30}, \bar{\omega}_{33}$, which happen to be positive in 2-D.
2. Four center points: $(l, m) = (1, 1), (1, 2), (2, 1), (2, 2)$.
   There are some positive contributions from the linear combinations of the

weights in the centered difference scheme; so we only need to show at each of these four center points, the positive weight of the bi-cubic interpolation minus the bi-linear interpolation weight is larger than zero. For the sake of symmetry, we only show that $\bar{\omega}_{11} - \omega_{11} > 0$, i.e., $\bar{\omega}_{11}^x \bar{\omega}_{11}^y - \omega_{11}^x \omega_{11}^y > 0$. Since $\bar{\omega}_{11}^x$, $\bar{\omega}_{11}^y$, ω_{11}^x, and ω_{11}^y are positive, it is enough to show that

$$\bar{\omega}_{11}^x > \omega_{11}^x \quad \text{and} \quad \bar{\omega}_{11}^y > \omega_{11}^y. \tag{3.13}$$

By straightforward computation, $\bar{\omega}_{11}^x = \frac{(\Delta x + a)(\Delta x - a)(2\Delta x - a)}{2\Delta x^3}$, $\omega_{11}^x = \frac{\Delta x - a}{\Delta x}$, $\bar{\omega}_{11}^y = \frac{(\Delta x + b)(\Delta x - b)(2\Delta x - b)}{2\Delta x^3}$, $\omega_{11}^y = \frac{\Delta x - b}{\Delta x}$. It is then straightforward to verify that (3.13) holds for any $0 < a < \Delta x$ and $0 < b < \Delta x$.

3. Eight edge points: $(l, m) = (1, 0), (2, 0), (0, 1), (0, 2), (1, 3), (2, 3), (3, 1), (3, 2)$. Again by symmetry we only need to show that the row entry corresponding to $(l, m) = (1, 0)$ is positive, i.e., $\frac{\omega_{11}}{\Delta x^2} + \frac{4\bar{\omega}_{10}}{\Delta x^2} > 0$, where $\omega_{11} > 0$, but $\bar{\omega}_{10} < 0$. So we need to show that $|\omega_{11}| > 4|\bar{\omega}_{10}|$, i.e., $|\omega_{11}^x \omega_{11}^y| > 4|\bar{\omega}_{10}^x \bar{\omega}_{10}^y|$. In fact we can show that

$$\omega_{11}^x > 6|\bar{\omega}_{10}^x|, \quad \text{and} \quad \omega_{11}^y \geq \frac{8}{9}|\bar{\omega}_{10}^y|. \tag{3.14}$$

Again by straightforward computation, $\omega_{11}^x = \frac{\Delta x - a}{\Delta x}$, $|\bar{\omega}_{10}^x| = \frac{a(\Delta x - a)(2\Delta x - a)}{6\Delta x^3}$, $\omega_{11}^y = \frac{\Delta x - b}{\Delta x}$, $|\bar{\omega}_{10}^y| = \frac{(\Delta x + b)(\Delta x - b)(2\Delta x - b)}{2\Delta x^3}$. Again one can straightforwardly verify that (3.14) holds for any $0 < a < \Delta x$ and $0 < b < \Delta x$.

Thus, Theorem 3.4 holds: the diagonal entries of $A^h = cI^h - M^h$ are all positive, the off-diagonal entries are all non-positive, and each row sums up to c. ■

REMARK 3.7. *The M-Matrix result of Theorem 3.4, at least for our particular parameter choices, does not hold in 3-D. The barycentric interpolation weights at the corners of the interpolation stencils are negative. A different convergence proof would be required. However, in practice we still observe second-order convergence in 3-D (Section 4.6).*

3.4. Numerical examples in $\mathbb{R}^2$.

3.4.1. Shifted Poisson's equation on the unit circle. We solve the shifted Poisson's equation $-\Delta_{\mathcal{S}} u + u = f$ on the unit circle $\mathcal{S}$; the exact solution is chosen as $\sin(\theta) + \sin(12\theta)$, and we compute the right-hand side function f from the exact solution. The discrete right-hand side is then obtained by evaluating the closest point extension of f at the grid points in the computational band. We construct $M^h = E_1^h L^h - \frac{4}{\Delta x^2}(I^h - E_3^h)$, and the coefficient matrix is $A^h = I^h - M^h$.

Since the embedding equation is a 2D problem, sparse direct solvers (e.g. Matlab's backslash) work well in solving the resulting linear system. After solving the linear system, we obtain the discrete solution defined on the banded grid points. To calculate the errors, we then place many sample points on $\mathcal{S}$, estimate the numerical solution at these points by cubic interpolation of the values at the surrounding grid points, and compute the ∞-norm of the errors at the sample points on $\mathcal{S}$. Table 3.1 shows second order convergence of the relative errors in the ∞-norm. Alternatively, the exact closest point extension of the exact solution can be performed onto the computational grid, and the errors can be directly calculated at the grid points; similar results are observed in this case.

3.4.2. Shifted Poisson's equation on a bean-shaped curve. Again we solve the shifted Poisson's equation $-\Delta_{\mathcal{S}} u + u = f$, but this time on a bean-shaped curve (see Figure 3.3).

Convergence study for the shifted Poisson's equation on a unit circle showing 2nd-order convergence.

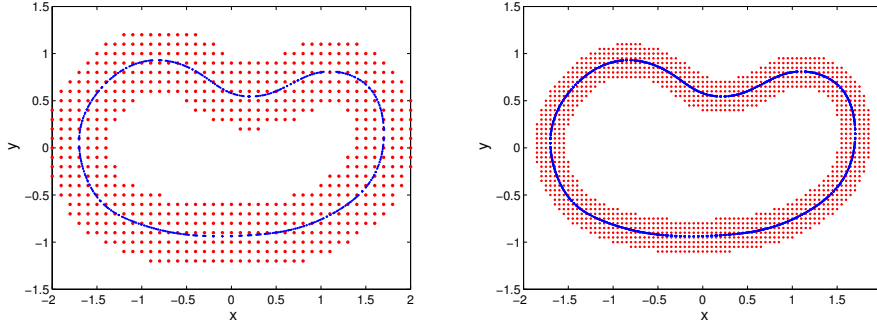| Δx	0.1	0.05	0.025	0.0125	0.00625	0.003125	0.0015625
$\frac{\|u-u^h\|_\infty}{\|u\|_\infty}$	6.51e-2	1.85e-2	4.76e-3	1.19e-3	2.97e-4	7.38e-5	1.85e-5
$\log_2 \frac{\|u-u^{2h}\|_\infty}{\|u-u^h\|_\infty}$		1.81	1.95	2.00	2.00	2.01	2.00

FIG. 3.3.   *Computational grids for the Closest Point Method on a bean-shaped curve with* $\Delta x = 0.1$ *(left) and* $\Delta x = 0.05$ *(right).*

This bean-shaped curve is constructed from a sequence of control points in $\mathbb{R}^2$; the Matlab function 'cscvn' [27] is used to get a parametric cubic spline curve passing through these points. This results in $(x(t), y(t))$ parameterized by $t \in [0, T]$. We obtain a closest point representation from this parametrization as follows: we fix a grid point, then construct the squared distance as a function of the parameter t. Next we minimize that function (over the parameter t) using Newton's method [3]. This is repeated for each grid point in the computational band.

We construct the exact solution in terms of the parametrization, $u(t) = \sin(\frac{2\pi}{T}t) + \sin(\frac{20\pi}{T}t)$. The Laplace–Beltrami operator of u in terms of this parametrization is $\Delta_{\mathcal{S}} u(t) = \frac{1}{\sqrt{\dot{x}(t)+\dot{y}(t)}} \frac{\mathrm{d}}{\mathrm{d}t} \left(\frac{1}{\sqrt{\dot{x}(t)+\dot{y}(t)}} \frac{\mathrm{d}u(t)}{\mathrm{d}t} \right)$. The right-hand side function is $f(t) = -\Delta_{\mathcal{S}} u(t) + u(t)$. Again we construct the discrete right-hand side and coefficient matrix, solve the resulting linear system to get the numerical solution, and compute the ∞-norm of the error on the bean-shaped curve. Table 3.2 shows second order convergence results.

Convergence study for the shifted Poisson's equation on a bean-shaped curve showing 2nd-order convergence.

Δx	0.1	0.05	0.025	0.0125	0.00625	0.003125	0.0015625
$\frac{\|u-u^h\|_\infty}{\|u\|_\infty}$	6.19e-2	1.17e-2	3.59e-3	8.77e-4	2.35e-4	5.32e-5	1.38e-5
$\log_2 \frac{\|u-u^{2h}\|_\infty}{\|u-u^h\|_\infty}$		2.40	1.71	2.03	1.90	2.14	1.95

4. V-Cycle Multigrid solver. In Section 3.4 we studied some numerical examples on curves in 2D, where the resulting linear systems were solved by sparse

direct solvers (e.g., Matlab's backslash). However, for problems where the embedding space is $\mathbb{R}^3$ or higher, iterative solvers are usually more desirable. Since the geometric multigrid method (see e.g., [4, 14]) is quite effective in solving linear systems arising from discretizations of elliptic operators, we combine it with the Closest Point Method to solve the linear system arising from the embedding equation corresponding to the surface elliptic PDEs.

4.1. The Multigrid "smoother": Jacobi iteration. One of the key ingredients of a Multigrid algorithm is the "smoother" [4, 14], which damps out high-frequency errors and thus smooths the solution at each grid level. One good choice of "smoother" is the Jacobi iteration: suppose we want to solve $A^h u^h = f^h$, starting from some initial u^h, we update the iterates by

$$u^h := u^h + \text{diag}(A^h)^{-1}(f^h - A^h u^h). \tag{4.1}$$

One possible approach is to simply use this standard Jacobi iteration on the discretization (3.3) of our embedding equation (2.5). We shall discuss this standard relaxation strategy further in Section 4.5.

An alternative strategy, and the one we propose here is based instead on considering the earlier constrained system (2.4): we want to ensure the solution satisfies the constraint (2.4b) so we re-extend the solution following each Jacobi iteration.

4.2. Ruuth–Merriman Jacobi iteration. The idea of this new smoothing strategy stems from the original Ruuth–Merriman approach for time-dependent surface PDEs [24]. In the continuous setting, if the solution $\tilde{u}$ is constant along the normal direction to the surface, then the Cartesian Laplacian of $\tilde{u}$ agrees with the Laplace–Beltrami function of $\tilde{u}$ on the surface. So roughly speaking $L^h u^h$ is consistent with $\Delta_S \tilde{u}$ *on the surface*, provided that u^h is constant along the normals to the surface. Under this side condition, we can replace M^h with L^h in one iteration. Let $\tilde{A}^h = cI^h - L^h$ be the shifted Cartesian Laplacian matrix. Starting from an initial u^h which is constant along the normal direction to the surface, in one iteration we do the standard Jacobi iteration with respect to the $\tilde{A}^h = cI^h - L^h$ (instead of $A^h = cI^h - M^h$), and then immediately do a closest point extension to ensure the discrete solution is still constant along the normal direction to the surface:

$$u^h := u^h + \text{diag}(\tilde{A}^h)^{-1}(f^h - \tilde{A}^h u^h), \tag{4.2a}$$
$$u^h := E^h u^h. \tag{4.2b}$$

We remark that interpolation E^h with sufficiently high degree should be used in order to avoid introducing interpolation errors which dominate over the errors from the discrete Laplacian L^h. In particular, we need to use cubic interpolation to build E^h if we use a second-order difference scheme to build L^h.

4.3. Restriction and prolongation operators. In a Multigrid algorithm, one also needs to build *restriction* operators which restrict data from fine grid to coarse grid and *prolongation* operators which prolong data from coarse grid to fine grid.

For practical efficiency, we would like to perform the computation in narrow bands with bandwidths shrinking proportional to the grid sizes. This makes the coarse grid band wider than the fine grid band (see Figure 4.1). Some coarse grid points are out of the range of the fine grid band, which means there are no fine grid points surrounding those "outer" coarse grid points; in those cases the standard restriction strategies such as "injection" and "full weighting" [4] do not work. We overcome this problem with

the help of the closest point extension. When restricting the values of points on the fine grid to the coarse grid, we assign the value of each coarse grid point to be the value of its corresponding closest point, which in turn is obtained by interpolating the values of fine grid points surrounding the closest point. Naturally, we can construct the prolongation operators in the same way:[3] take the value of each fine grid point to be the value of its corresponding closest point, which is obtained through interpolation of values of coarse grid points. Similarly to the closest point extension on a single grid, the restriction and prolongation operators have corresponding matrix forms; we denote the restriction matrix by E_h^{2h}, and the prolongation matrix by E_{2h}^h. Figure 4.1 illustrates the process of doing restriction and prolongation.
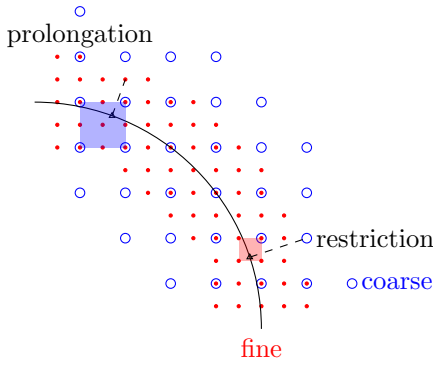

FIG. 4.1.   *Illustration of Restriction and Prolongation. Blue circles indicate the coarse grid points, red dots indicate the fine grid points.*
Restriction: restrict quantities from fine grid to coarse grid using E_h^{2h}.
Prolongation: prolong quantities from coarse grid to fine grid using E_{2h}^h.

4.4. Closest Point Method V-Cycle algorithm. Armed with the smoothing strategy in Section 4.2 and the construction of the restriction and prolongation operators in Section 4.3, we propose the Closest Point Method Multigrid algorithm. In this paper, we use the simplest V-Cycle Multigrid scheme, although the results could be extended to more general Multigrid schemes such as W-Cycle or the full Multigrid schemes. We remark that this algorithm does not explicitly involve the side condition as in (2.5), but instead follows each iteration with a closest point extension as in the original Ruuth–Merriman approach [24].

ALGORITHM 4.1 (Closest Point Method V-Cycle Algorithm). *Denote by B^h and B^{2h} the fine and next coarser grids. Denote by E^h and E^{2h} the extension matrices on the fine and next coarser grids (see Sec. 3.1). Denote the shifted Cartesian Laplacian matrix, the solution and right-hand side on the fine grid by $\tilde{A}^h = cI^h - L^h$, u^h, and f^h, and the corresponding variables on the next coarser grid by $\tilde{A}^{2h} = cI^{2h} - L^{2h}$, u^{2h}, and f^{2h}. Let E_h^{2h} and E_{2h}^h be the restriction and prolongation matrices (which are also extensions as in Sec. 4.3). We compute $u^h = V^h(u^h, f^h)$ by recursively calling:*

1. *Starting from some initial guess u^h which is constant along the normals to the surface (e.g. $u^h = 0^h$) on the finest grid, do ν_1 steps of Jacobi iteration with respect to $\tilde{A}^h$, each step followed by a closest point extension:*

$$for\ i = 1 : \nu_1,\ do$$
$$u^h := u^h + diag(\tilde{A}^h)^{-1}(f^h - \tilde{A}^h u^h);$$
$$u^h := E^h u^h.$$

---

[3]An alternative approach is simply to use one of the standard nest-grid multigrid approaches (although we have not tested this here).

2. *Compute the residual and restrict it to the coarser grid,*

$$r^h := f^h - \tilde{A}^h u^h, \tag{4.3}$$
$$f^{2h} := E_h^{2h} r^h,$$

If $B^{2h} = $ coarsest grid, solve $A^{2h} u^{2h} = f^{2h}$ directly; else

$$u^{2h} := 0^{2h},$$
$$u^{2h} := V^{2h}(u^{2h}, f^{2h}).$$

3. *Correct the fine grid solution by coarse grid solution:*

$$u^h := u^h + E_{2h}^h u^{2h}.$$

4. *Do ν_2 steps of Jacobi iteration with respect to $\tilde{A}^h$, each step followed by a closest point extension:*

$$for\ i = 1 : \nu_2,\ do$$
$$u^h := u^h + diag(\tilde{A}^h)^{-1}(f^h - \tilde{A}^h u^h);$$
$$u^h := E^h u^h.$$

4.5. An alternative relaxation strategy. In Step 1 and Step 4, instead of using the Ruuth–Merriman smoothing strategy (4.2a) and (4.2b), one can simply use the iteration scheme (4.1) which only depends on the linear system $A^h u^h = f^h$. One can also easily replace the smoother based on Jacobi iteration with other iteration methods (e.g., Gauss–Seidel iteration). When applying this standard relaxation strategy, we found that replacing the residual calculation (4.3) with $r^h = f^h - A^h(E^h u^h)$ helps to maintain the desired convergence rate of the V-Cycle scheme. This extra extension has no effect in the continuous setting but seems to improve the convergence rate of the discrete algorithm.

Even with this modified residual calculation, we sometimes observed slightly faster convergence results using the Ruuth–Merriman smoothing strategy. Thus for the remainder of this work, we use the Ruuth–Merriman smoothing strategy.

4.6. Numerical examples. We test our V-Cycle solver for the shifted Poisson's equation on several closed curves in $\mathbb{R}^2$ and surfaces in $\mathbb{R}^3$. We use cubic (degree 3) interpolations to construct E^h's on each grid level. In each round of the V-Cycle, $\nu_1 = 3$ pre-smoothings and $\nu_2 = 3$ post-smoothings are applied. For the restriction and prolongation operators, linear (degree 1) interpolations are used for the closest point extensions. The linear system on the coarsest grid level is solved by Matlab's backslash. The stopping criteria for all the tests are $\|x^{k+1} - x^k\|_\infty / \|x^k\|_\infty < 10^{-6}$, where x^k and x^{k+1} are the iterative solutions after the k-th and $(k+1)$-th rounds of V-Cycles.

4.6.1. Unit circle. We consider the simplest example from Section 3.4.1, where we solve the shifted Poisson's equation $-\Delta_\mathcal{S} u + u = f$ on the unit circle. The exact solution is chosen as $\sin(\theta) + \sin(12\theta)$.

To test the convergence rate of our multigrid solver, we keep the coarsest grid size unchanged, and reduce the finest grid size. Figure 4.2(a) shows the decreasing rate of the residuals of the algebraic linear systems, and Figure 4.2(b) shows the decreasing rate of the numerical errors. Before the numerical solutions achieve the stopping criterion, they have already reached the limit of the discretization errors,

and the errors will not decrease after that; so in Figure 4.2(b) as the number of V-Cycles increases, the errors first decrease and then stay almost the same. This same behaviour is also observed in the residuals in Figure 4.2(a): as the number of V-Cycles increases, the residuals initially decrease. However, because we introduce additional discretization errors to the original linear system $A^h u^h = f^h$ (by performing discrete closest point extensions after each smoothing step), the residuals eventually stagnate at the level of this additional discretization error. In both Figures 4.2(a) and 4.2(b), the rate of decrease (the slope of the lines) stays almost the same as we refine the finest mesh, which is expected and desirable in a multigrid algorithm.
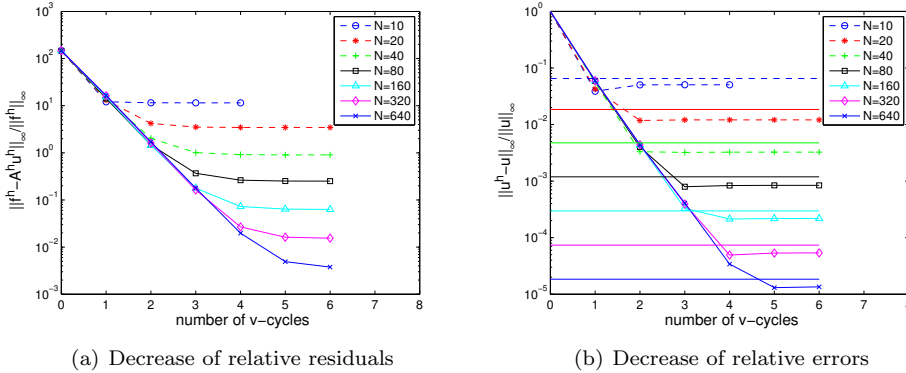

(a) Decrease of relative residuals

(b) Decrease of relative errors

FIG. 4.2.   *Convergence results on a circle, where the curves show a sequence of progressively finer grids, each solved with the V-Cycle multigrid method. Each curve shows how the relative residuals/errors decrease as the number of V-Cycles increases. Here $N = \frac{1}{\Delta x}$, where Δx is the grid size of the finest mesh for that curve. The coarsest grid in each case corresponds to $N = 5$. The horizontal lines in (b) are the numerical errors given by Matlab's backslash.*

4.6.2. Bean-shaped curve. We test the shifted Poisson's equation on the bean-shaped curve as in Section 3.4.2, and the same exact solution is chosen for convergence studies. Figure 4.3(a) shows the numerical solution for the embedding equation with meshsize $\Delta x = 0.1$. Figure 4.3(b) shows the convergence results of the multigrid method. Note again that the convergence rate (slope of lines) is essentially independent of the finest grid size.

4.6.3. Unit sphere. To make an exact solution and perform a convergence study, we parameterize a sphere in the spherical coordinates (θ, ϕ, r): $x = r \sin \phi \cos \theta$, $y = r \sin \phi \sin \theta$, $z = r \cos \phi$, where θ is the azimuth ranging from 0 to 2π, ϕ is the elevation from 0 to π, and r is the radius.

We emphasize this parametrization is not used in our algorithm: it is only used to compute the error. For simplicity, we solve the equation on a unit sphere centered at the origin, and choose the exact solution as the spherical harmonic $u(\theta, \phi) = \cos(3\theta) \sin(\phi)^3 (9 \cos(\phi)^2 - 1)$. The right-hand side function is $-\Delta_\mathcal{S} u + u = -29u(\theta, \phi)$. Figure 4.4(a) shows the numerical solution for the embedding equation with grid size $\Delta x = 0.1$, visualized using the parametrization. Figure 4.4(b) shows the convergence results of the multigrid method.

Besides convergence studies, we also investigate the computational cost including the degrees of freedom and matrix storage for the discrete linear system (see Table 4.1). Because our 3D computation is performed in a narrow band with bandwidth propor-
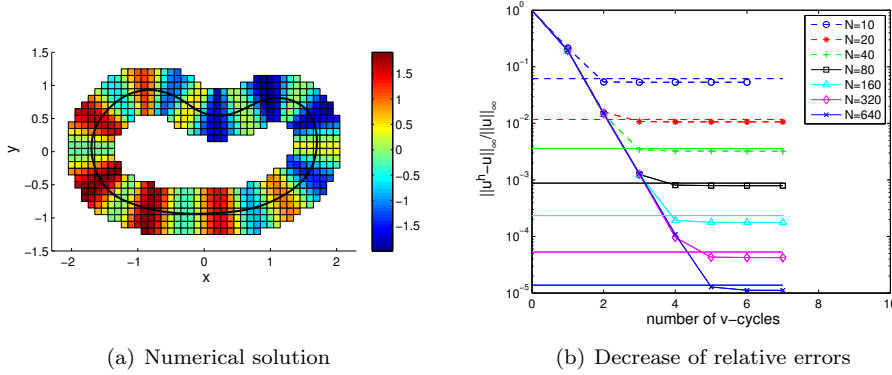
(a) Numerical solution

(b) Decrease of relative errors

FIG. 4.3.   *V-Cycle convergence results on a bean shaped curve. The horizontal lines in figure (b) are the numerical errors given by Matlab's backslash.*
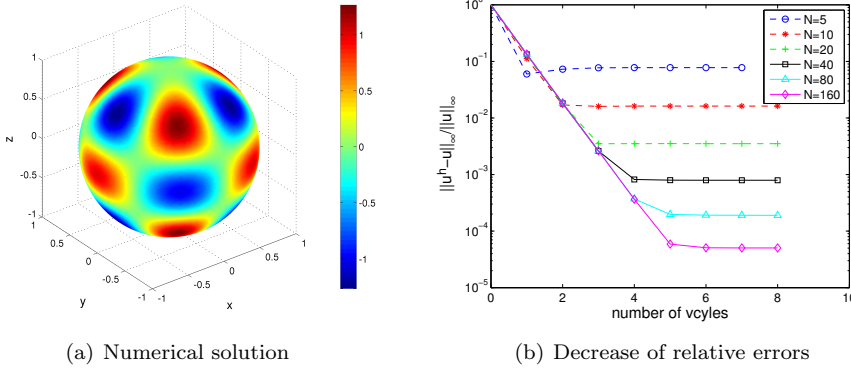

(a) Numerical solution

(b) Decrease of relative errors

FIG. 4.4.   *V-Cycle convergence results on a unit sphere.*

tional to the mesh size Δx, the number of degrees of freedom scales like $O(\Delta x^{-2})$, just as if we performed a finite difference method to solve the Poisson's equation in $\mathbb{R}^2$. Since we use the standard 7-point stencil, the number of nonzero entries (nnz) of the Laplacian matrix L^h is about 7 times the number of degrees of freedom. Since we use degree 3 polynomial interpolation in a dimension by dimension fashion, the number of nonzero entries of the interpolation matrix E_3^h is about $4^3 = 64$ times the number of degrees of freedom. The matrix $\tilde{A}^h$ used in our Ruuth–Merriman smoothing approach is simply the diagonally shifted Laplacian so $\mathrm{nnz}(\tilde{A}^h) = \mathrm{nnz}(L^h)$. From the analysis in Section 3.3, M^h has nearly the same sparsity pattern as E_3^h, except that M^h might have more diagonal entries than E_3^h, so the number of nonzero entries of M^h is about 64 or 65 times the number of degrees of freedom.

We also compare the CPU times for solving the linear system by Matlab's backslash and our V-Cycle multigrid scheme. Table 4.2 shows the performance comparison. Computations were performed on a 3.47 GHz Intel Xeon X5690 6-core processor, with 100 GB memory. For the smallest problem, Matlab's backslash works better than multigrid; but for larger problems, multigrid works better. What is more, the CPU time of multigrid scales roughly as $O(\Delta x^{-2})$, i.e., proportional to the number of

TABLE 4.1

Computational cost for the Closest Point Method on a sphere. As we decrease the mesh size by a factor of 2, the number of degrees of freedom (DOFs, i.e., length(u^h)) increases by a factor of 4. $nnz(L^h) \approx 7 \times DOFs$, $nnz(E^h) \approx 64 \times DOFs$, $nnz(M^h) \approx 64.5 \times DOFs$.

Δx	length(u^h)	nnz(L^h)	nnz(E_3^h)	nnz(M^h)
0.2	3190	20758	204160	205686
0.1	10906	71962	697984	702714
0.05	41870	277358	2679680	2697038
0.025	166390	1103734	10648960	10717230
0.0125	663454	4402366	42461056	42731646
0.00625	2651254	17593318	169680256	170760222

degrees of freedom, which is optimal and what we expect for a multigrid scheme [4].

Δx	Backslash	V-Cycle
0.2	0.169	0.294
0.1	1.046	0.551
0.05	6.967	1.326
0.025	59.94	4.377
0.0125	466.5	16.66
0.00625	N/A	67.42

TABLE 4.2

CPU time for solving the linear system arising from the Poisson's equation on a unit sphere with the Closest Point Method. Matlab's backslash versus V-Cycle multigrid method.

4.6.4. Torus. Again, to calculate an exact solution, we begin with a parametrization of a torus: $x(\theta, \phi) = (R + r \cos \phi) \cos \theta$, $y(\theta, \phi) = (R + r \cos \phi) \sin \theta$, $z(\theta, \phi) = r \sin \phi$, where ϕ, θ are in the interval $[0, 2\pi)$, R is the distance from the center of the tube to the center of the torus, and r is the radius of the tube.

We test the shifted Poisson's equation $-\Delta_{\mathcal{S}} u + u = f$ on a torus with $R = 1.2$, and $r = 0.6$. The exact solution is chosen as $u(\theta, \phi) = \sin(3\theta) + \cos(2\phi)$, and the right hand side function is $f(\theta, \phi) = \frac{9 \sin(3\theta)}{(R + r \cos \phi)^2} - \frac{2 \sin \phi \sin(2\phi)}{r(R + r \cos \phi)} + \frac{4 \cos(2\phi)}{r^2} + u(\theta, \phi)$. Figure 4.5 shows the numerical solution and the multigrid convergence results.

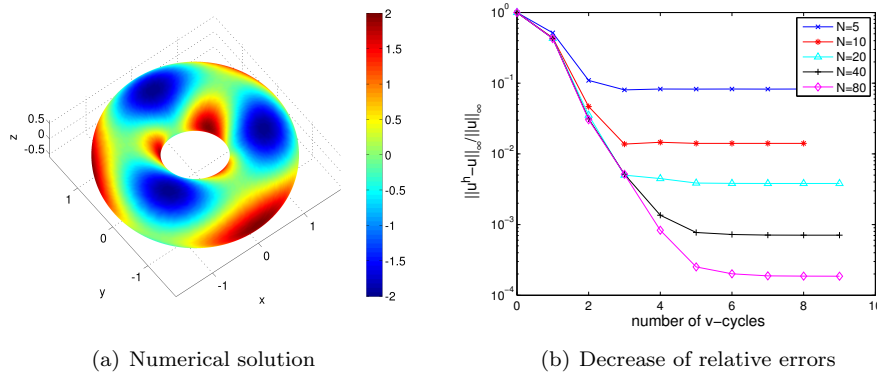(a) Numerical solution   (b) Decrease of relative errors

FIG. 4.5.   *V-Cycle convergence results on a torus.*

4.6.5. A level set example. Following Dziuk [7], we consider the surface defined by $\mathcal{S} = \{ \boldsymbol{x} \in \mathbb{R}^3 \mid (x_1 - x_3^2)^2 + x_2^2 + x_3^2 = 1 \}$, and the shifted Poisson's equation

$-\Delta_{\mathcal{S}} u + u = f$ on $\mathcal{S}$. The exact solution is chosen to be $u(\boldsymbol{x}) = x_1 x_2$. We compute the right-hand side function by $f = -\nabla_{\mathcal{S}} \cdot \boldsymbol{v}$, where $\quad \boldsymbol{v} = \nabla_{\mathcal{S}} u = \nabla u - (\nabla u \cdot \boldsymbol{n}) \boldsymbol{n}$, and $\nabla_{\mathcal{S}} \cdot \boldsymbol{v} = \nabla \cdot \boldsymbol{v} - \sum_{j=1}^{3} (\nabla \boldsymbol{v}_j \cdot \boldsymbol{n}) \boldsymbol{n}_j$. Here $\boldsymbol{n}$ is the normal vector, and in this case, $\boldsymbol{n}(\boldsymbol{x}) = \left(x_1 - x_3^2, \ x_2, \ x_3(1 - 2(x_1 - x_3^2)) \right) / \left(1 + 4x_3^2(1 - x_1 - x_2^2) \right)^{1/2}$. For each grid point, we compute the closest point on $\mathcal{S}$ by minimizing the squared distance function using Newton's method. Figure 4.6 shows the numerical solution and multigrid convergence results.
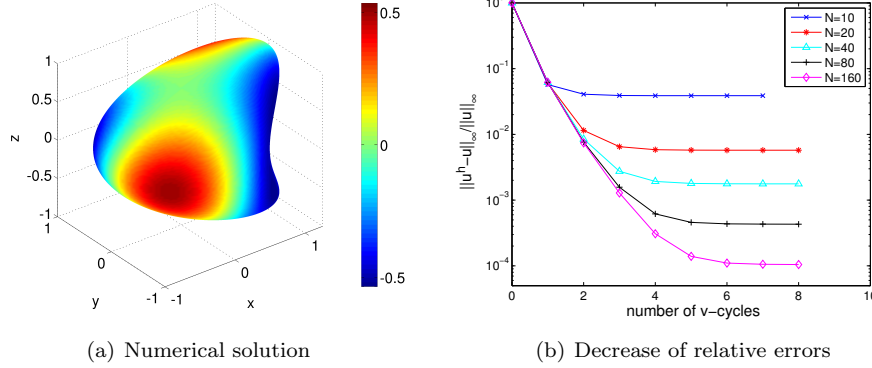

(a) Numerical solution   (b) Decrease of relative errors

FIG. 4.6.   *V-Cycle convergence results on the Dziuk surface.*

4.6.6. Elliptic equation with variable diffusion coefficients on a sphere. Finally, we consider an example with scalar variable diffusion coefficients, $-\nabla_{\mathcal{S}} \cdot (a(\boldsymbol{y}) \nabla_{\mathcal{S}} u(\boldsymbol{y})) + c u(\boldsymbol{y}) = f(\boldsymbol{y})$, for $\boldsymbol{y} \in \mathcal{S}$.

To formulate the continuous embedding equation, we simply choose $\boldsymbol{A}(\mathrm{cp}(\boldsymbol{x})) = a(\mathrm{cp}(\boldsymbol{x}))$ in the general embedding equation (2.9), and get $-[\nabla \cdot (a(\mathrm{cp}(\boldsymbol{x})) \nabla \tilde{u})](\mathrm{cp}(\boldsymbol{x})) + c\tilde{u}(\boldsymbol{x}) + \gamma(\tilde{u}(\boldsymbol{x}) - \tilde{u}(\mathrm{cp}(\boldsymbol{x}))) = \tilde{f}(\boldsymbol{x})$ for $\boldsymbol{x} \in B(\mathcal{S})$. Similar to the Poisson case before, this embedding equation can be discretized using standard finite differences and interpolation schemes, see also [31]. The matrix formulation of the discretization is $-E^h \tilde{L}^h u^h + \gamma(I^h - E^h) u^h = f^h$, where $\tilde{L}^h = \boldsymbol{D}_x^b \mathrm{diag}(\boldsymbol{A}_x^f a^h) \boldsymbol{D}_x^f + \boldsymbol{D}_y^b \mathrm{diag}(\boldsymbol{A}_y^f a^h) \boldsymbol{D}_y^f + \boldsymbol{D}_z^b \mathrm{diag}(\boldsymbol{A}_z^f a^h) \boldsymbol{D}_z^f$. Here we have used similar notations to those in [31]. $\boldsymbol{D}_x^b$ is the matrix corresponding to backward differences in the x direction, $\boldsymbol{D}_x^f$ is the matrix corresponding to forward differences in the x direction; $\boldsymbol{D}_y^b$, $\boldsymbol{D}_y^f$, $\boldsymbol{D}_z^b$ and $\boldsymbol{D}_z^f$ have similar meanings. The column vector a^h has the i-th entry equal to $a(\mathrm{cp}(\boldsymbol{x}_i))$, where $\boldsymbol{x}_i$ is the i-th grid point. $\boldsymbol{A}_x^f$ is the forward averaging matrix corresponding to calculating the average of two neighboring values of a^h along the positive x direction. $\boldsymbol{A}_x^f a^h$ is a column vector and $\mathrm{diag}(\boldsymbol{A}_x^f a^h)$ is a diagonal matrix with diagonal entries equal to $\boldsymbol{A}_x^f a^h$; $\mathrm{diag}(\boldsymbol{A}_y^f a^h)$ and $\mathrm{diag}(\boldsymbol{A}_z^f a^h)$ have similar meanings.

In the multigrid algorithm, we continue to use the Ruuth–Merriman style relaxation strategy, except changing L^h to $\tilde{L}^h$.

We test on a unit sphere. We choose the exact solution $u(\phi) = \cos \phi$, diffusion coefficient $a(\phi) = \cos \phi + 1.5$, and the right hand side function is $f(\phi) = 2 \cos \phi (\cos \phi + 1.5) - (\sin \phi)^2 + u(\phi)$. The multigrid convergence results are shown in Figure 4.7 and look similar to the Poisson problems shown earlier.

5. Conclusions. We adapt the Closest Point Method to solve elliptic PDEs on surfaces. In particular, we analyze the shifted Poisson's equation $-\Delta_{\mathcal{S}} u + c u = f$ in

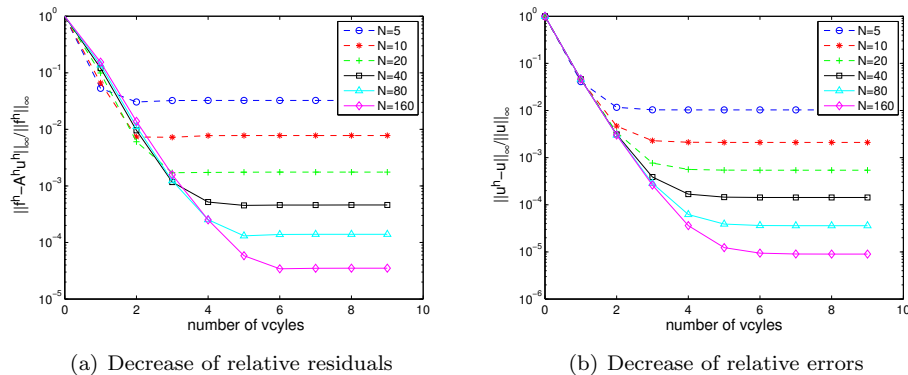(a) Decrease of relative residuals   (b) Decrease of relative errors

FIG. 4.7. *V-Cycle convergence results for a variable diffusion coefficient example.*

detail. We formulate an embedding equation which includes a *consistency condition* from the surface PDE and a *side condition* to enforce the solution to be constant along the normals to the surface. We then discretize the embedding equation using standard centered finite difference methods and Lagrange interpolation schemes. We prove the convergence for the difference scheme in a simple case where the underlying surface is a closed curve embedded in $\mathbb{R}^2$.

We then propose a specific geometric multigrid method to solve the resulting large sparse linear system. The method makes full use of the closest point representation of the surface and uniform Cartesian grids in different levels. Numerical tests suggest that the convergence speeds do not deteriorate as we increase the number of grid levels while fixing the size of the coarsest grid, just as if we performed a standard multigrid algorithm for the (Cartesian) Laplacian operator.

There are many other possible multigrid methods; in particular, Section 4.5 mentions an alternative approach based directly on our modified equation (which additively combines the side and consistency conditions). Future work could investigate this further.

Numerical results in Section 4.6.6 show that our approach also works for non-constant coefficient elliptic PDEs with scalar diffusivity $a(\boldsymbol{y})$. It would be useful for some applications to investigate more general elliptic PDEs, replacing $a(\boldsymbol{y})$ with a symmetric and semi-positive definite diffusivity matrix $\boldsymbol{A}(\boldsymbol{y})$. Our approach should work here too although we have not tested it.

Finally, our analysis of the spatial discretizations of elliptic operators can be used to analyze embedded method-of-lines approaches for parabolic PDEs on general surfaces [31].

REFERENCES

[1] J.-P. BERRUT AND L. N. TREFETHEN, *Barycentric Lagrange interpolation*, SIAM Rev., 46 (2004), pp. 501–517.
[2] M. BERTALMÍO, L.-T. CHENG, S. OSHER, AND G. SAPIRO, *Variational problems and partial differential equations on implicit surfaces*, J. Comput. Phys., 174 (2001), pp. 759–780.
[3] S. BOYD AND L. VANDENBERGHE, *Convex Optimization*, Cambridge University Press, 2004.
[4] W. L. BRIGGS, V. E. HENSON, AND S. F. MCCORMICK, *A Multigrid Tutorial*, SIAM, second ed., 2000.

[5] M. Burger, *Finite element approximation of elliptic partial differential equations on implicit surfaces*, Comp. Vis. Sci., 12 (2009), pp. 87–100.

[6] K. Deckelnick, G. Dziuk, C. M. Elliott, and C.-J. Heine, *An h-narrow band finite-element method for elliptic equations on implicit surfaces*, Journal of Numerical Analysis, 30 (2009), pp. 351–376.

[7] G. Dziuk, *Finite elements for the Beltrami operator on arbitrary surfaces*, Lecture Notes in Mathematics, 1357 (1988), pp. 142–155.

[8] G. Dziuk and C. M. Elliott, *Surface finite elements for parabolic equations*, Journal of Computational Mathematics, 25 (2007), p. 385.

[9] G. Dziuk and C. M. Elliott, *Eulerian finite element method for parabolic PDEs on implicit surfaces*, Interfaces and Free Boundaries, 10 (2008), pp. 119–138.

[10] ———, *An Eulerian level set method for partial differential equations on evolving surfaces*, Comput. Vis. Sci., 13 (2008), pp. 17–28.

[11] M. S. Floater and K. Hormann, *Surface parameterization: a tutorial and survey*, in Advances in Multiresolution for Geometric Modelling, Springer, 2005, pp. 157–186.

[12] E. J. Fuselier and G. B. Wright, *A high-order kernel method for diffusion and reaction-diffusion equations on surfaces*, (2012). arXiv:1206.0047.

[13] J. B. Greer, *An improvement of a recent Eulerian method for solving PDEs on general geometries*, J. Sci. Comput., 29 (2006), pp. 321–352.

[14] W. Hackbusch, *Multi-Grid Methods and Applications*, Springer, 2003.

[15] M. W. Hirsch, *Differential Topology*, Springer-Verlag, 1976.

[16] J. Liang and H.-K. Zhao, *Solving partial differential equations on point clouds*, (2012). CAM Report 12-25, UCLA, Mathematics Department.

[17] C. B. Macdonald, J. Brandman, and S. J. Ruuth, *Solving eigenvalue problems on curved surfaces using the Closest Point Method*, J. Comput. Phys., 230 (2011), pp. 7944–7956.

[18] C. B. Macdonald, B. Merriman, and S. J. Ruuth, *Simple computation of reaction-diffusion processes on point clouds*, Proc. Natl. Acad. Sci., 110 (2013).

[19] C. B. Macdonald and S. J. Ruuth, *Level set equations on surfaces via the Closest Point Method*, J. Sci. Comput., 35 (2008), pp. 219–240. doi:10.1007/s10915-008-9196-6.

[20] ———, *The implicit Closest Point Method for the numerical solution of partial differential equations on surfaces*, SIAM J. Sci. Comput., 31 (2009), pp. 4330–4350. doi:10.1137/080740003.

[21] T. März and C. B. Macdonald, *Calculus on surfaces with general closest point functions*, SIAM J. Numer. Anal., 50 (2012), pp. 3303–3328.

[22] L. Olsen, P. K. Maini, and J. A. Sherratt, *Spatially varying equilibria of mechanical models: Application to dermal wound contraction*, Math. BioSci., 147 (1998), pp. 113–129.

[23] C. Piret, *The orthogonal gradients method: a radial basis functions method for solving partial differential equations on arbitrary surfaces*, J. Comput. Phys., (2012).

[24] S. J. Ruuth and B. Merriman, *A simple embedding method for solving partial differential equations on surfaces*, J. Comput. Phys., 227 (2008), pp. 1943–1961.

[25] H. A. Stone, *A simple derivation of the time-dependent convective-diffusion equation for surfactant transport along a deforming interface*, Phys. Fluids A, 2 (1989), p. 111.

[26] P. Tang, F. Qiu, H. Zhang, and Y. Yang, *Phase separation patterns for diblock copolymers on spherical surfaces: A finite volume method*, Phys. Rev. E, 72 (2005).

[27] The MathWorks, Inc, *Natural or periodic interpolating cubic spline curve (Matlab documentation)*. http://www.mathworks.co.uk/help/toolbox/curvefit/cscvn.html.

[28] L. Tian, C. B. Macdonald, and S. J. Ruuth, *Segmentation on surfaces with the closest point method*, Proc. ICIP09, International Conference on Image Processing, Cairo, Egypt, (2009).

[29] G. Turk, *Generating textures on arbitrary surfaces using reaction-diffusion*, SIGGRAPH Comput. Graph., 25 (1991), pp. 289–298.

[30] J. M. Varah, *A lower bound for the smallest singular value of a matrix*, Linear Algebra and its Applications, 11 (1975), pp. 3–5.

[31] I. von Glehn, T. März, and C. B. Macdonald, *An embedded method-of-lines approach to solving partial differential equations on surfaces*, (2013). Submitted.

[32] J.-J. Xu and H.-K. Zhao, *An Eulerian formulation for solving partial differential equations along a moving interface*, J. Comput. Phys., 19 (2003), pp. 573–594.